Critical evaluation of attosecond time delays retrieved from photoelectron streaking measurements

Hui Wei,[1,*] Toru Morishita,[2] and C. D. Lin[1]

[1]*J. R. Macdonald Laboratory, Department of Physics, Kansas State University, Manhattan, Kansas 66506, USA*

[2]*Institute for Advanced Science, The University of Electro-communications 1-5-1 Chofu-ga-oka, Chofu-shi, Tokyo 182-8585, Japan*

A photoelectron streaking experiment which was conceived as a means to extract the electron wave packet of single-photon ionization has also been employed to retrieve time delays in the fundamental photoemission processes. The discrepancies between the time delays thus measured and those from many sophisticated theoretical calculations have generated a great deal of controversy in recent years. Here we present a careful examination of the methods that were used to retrieve the time delays and demonstrate the difficulty of achieving an accuracy of the retrieved time delays of a few to tens of attoseconds in typical streaking measurements. The difficulty owes more to the lower sensitivity of the streaking spectra to the phase of the photoionization transition dipole than to the spectral phase of the attosecond light pulse in the experiment. The retrieved time delay contains extra errors when the attochirp of the attosecond pulse is large so that the dipole phase becomes negligible compared to it.

I. INTRODUCTION

Photoelectron spectroscopy is a standard tool for probing the structure of matter. In conventional photoionization measurements accurate values of the amplitude of the complex single-photon transition dipole matrix element can be readily obtained but its phase is not available. For years, the calculated dipole phase has been used to define the so-called Eisenbud-Wigner-Smith-type time delay [1–3] (we call it the Wigner delay for short), which is obtained by taking the energy derivative of the dipole phase. The original Wigner delay was introduced for a system with a short-range potential, however, this concept has been generalized to include the Coulomb phase shift [4]. Wigner time delays are usually on the attosecond (as) scale, thus it may be possible to probe them using extreme ultraviolet (XUV) attosecond pulses.

To determine either the phase of the XUV or the transition dipole requires a nonlinear process, such as XUV photoionization in the presence of a delayed femtosecond infrared (IR) field. When their relative time delays are swept, the electron spectrum shifts (streaks) in relation to the optical cycle of the IR. The collection of the streaked spectra is called a spectrogram. So far such streaking experiments have been reported for atoms, molecules, and condensed matter in numerous experiments [5–11]. Despite these activities, what information on the structure or the photoionization dynamics of the target can be extracted from these experiments is still rather unclear.

In this article, we focus on the *photoionization time delay* of atoms. This topic has generated a great deal of controversy since the first experiment, by Schultze *et al.* [9] in 2010, where a "time delay" of 21 as was reported between the ionization from the 2*p* and that from the 2*s* subshells of Ne. A flurry of theoretical works [12–17], plus two tutorials [18,19] and one recent article [4], have all been devoted to "getting" this number. As the authors of the article stated (p. 766), "Precisely which information is actually encoded and how it can be retrieved...is still a widely open question."

To address this open question, in this article we take a fresh look at the main method of extracting temporal information from the streaking spectrogram: the FROG-CRAB (frequency-resolved optical gating for complete reconstruction of attosecond bursts) [20,21] method. Note that the "time delay" is not an actually measured quantity or a fundamental parameter in the quantum theory of photoionization. The FROG-CRAB method actually extracts the phase (difference) of the transition dipole from which the time delay is derived. In Sec. II we briefly introduce the FROG-CRAB method, which is based on the strong-field approximation (SFA). We also discuss how accurate transition dipoles are calculated theoretically. In Sec. III we use the SFA model to generate photoelectron spectrograms and apply the FROG-CRAB algorithm to retrieve the time delay between the photoionization from Ne 2*p* and that from Ne 2*s* subshells or the time delay between the ionization from Ar and that from Ne. We use different XUV pulses to generate the spectrogram and check the performance of the FROG-CRAB method against the XUV chirp or bandwidth. Due to the limitation of FROG-CRAB, in Sec. IV we propose a fitting approach to extract the dipole phase and Wigner delay of Ar by using Ne as the reference target. In Sec. V we check the accuracy of the SFA model for low-energy photoelectrons by comparing the spectrograms obtained by SFA and by solving the time-dependent Schrödinger equation (TDSE) numerically. We also show the error of FROG-CRAB in the XUV or dipole phase retrieval when using TDSE spectrograms as the input. Finally, in Sec. VI we summarize and discuss the general issues of extracting atomic dipole phases using laser-assisted photoionization with single attosecond pulses. Atomic units are used in this paper unless otherwise stated.

II. STRONG-FIELD APPROXIMATION MODEL AND FROG-CRAB METHOD

According to the FROG-CRAB method, a so-called "photoelectron wave packet" as well as the IR field can be retrieved from the spectrogram. It is assumed that the spectrogram can

―――――
*huiwei@phys.ksu.edu

be modeled by the SFA [22]:

$$S(p,\tau) = \left| \int_{-\infty}^{\infty} E_{\text{XUV}}(t-\tau)d[p+A(t)] \right.$$
$$\left. \times e^{-i\varphi(p,t)}e^{i(\frac{p^2}{2}+I_p)t}dt \right|^2. \quad (1)$$

Here the polarizations of the XUV, the IR, and the photoelectrons are all taken along the $+z$ direction. In Eq. (1), p is the asymptotic momentum of the photoelectron, and then the energy of the electron $E = p^2/2$. τ is the relative temporal shift between the two fields. $A(t)$ is the vector potential of the IR, $E_{\text{IR}}(t) = -\frac{\partial}{\partial t}A(t)$. The function $\varphi(p,t)$ reads

$$\varphi(p,t) = \int_{t}^{\infty}\left[pA(t') + \frac{1}{2}A^2(t')\right]dt'. \quad (2)$$

The XUV pulse can be expressed as

$$E_{\text{XUV}}(t) = \sqrt{I(t)}\cos[\Omega_0 t + \zeta(t)], \quad (3)$$

in which Ω_0 is its central frequency, $I(t)$ is its temporal intensity envelope, and $\zeta(t)$ is the temporal phase including attochirps.

Equation (1) includes the single-photon transition dipole by the XUV, $d(p) = \langle p\hat{z}|z|i\rangle$, where $|i\rangle$ is the initial bound state with ionization potential I_p. In the standard SFA, the continuum state $|p\hat{z}\rangle$ is approximated by a plane-wave state e^{ipz}, but here we follow the earlier usage [22], where $|p\hat{z}\rangle$ is the accurate scattering wave function, which is a continuum eigenstate of the field-free Hamiltonian with asymptotic momentum $p\hat{z}$. In this work we use single-active-electron (SAE) model potentials for atoms given by Tong and Lin [23], which have the form

$$V(r) = -\frac{Z_c + a_1 e^{-a_2 r} + a_3 r e^{-a_4 r} + a_5 e^{-a_6 r}}{r}. \quad (4)$$

Here $Z_c = 1$ is the asymptotic charge seen by the active electron for neutral atoms. We can solve the field-free Schrödinger equation numerically to obtain the bound and continuum wave functions. The initial state has well-defined angular momentum quantum number l_i such that

$$\langle \mathbf{r}|i\rangle = \frac{u_i(r)}{r}Y_{l_i m_i}(\theta,\phi), \quad (5)$$

where m_i is the magnetic quantum number, and $u_i(r)$ is the normalized radial wave function of the initial state. $Y_{lm}(\theta,\phi)$ is the well-known spherical harmonics. The continuum state $|p\hat{z}\rangle$ can be constructed by partial waves as [24]

$$\langle \mathbf{r}|p\hat{z}\rangle = \sum_{l=0}^{\infty} e^{-i\eta_l(E)}\sqrt{\frac{2l+1}{4\pi}}\frac{u_{El}(r)}{r}Y_{l0}(\theta,\phi). \quad (6)$$

The energy normalized radial wave function $u_{El}(r)$ has the asymptotic form

$$\lim_{r\to\infty} u_{El}(r) = \sqrt{\frac{2}{\pi p}}\sin\left(pr + \frac{Z_c}{p}\ln(2pr) + \eta_l(E)\right), \quad (7)$$

and

$$\eta_l(E) = -\frac{l\pi}{2} + \sigma_l(E) + \delta_l(E), \quad (8)$$

where $\sigma_l = \arg[\Gamma(l+1-iZ_c/p)]$ is the Coulomb phase shift and δ_l is the short-range phase shift due to the short-range deviation from a pure Coulomb potential.

For photoionization from s states ($l_i = 0$), the transition dipole involves the continuum p wave only,

$$d(E) = -i\sqrt{\frac{1}{4\pi}}e^{i[\sigma_1(E)+\delta_1(E)]}\langle u_{E1}|r|u_i\rangle; \quad (9)$$

however, for photoionization from p states ($l_i = 1$), the transition dipole involves both the continuum s-wave and the continuum d-wave,

$$d(E) = \sqrt{\frac{1}{12\pi}}\{e^{i[\sigma_0(E)+\delta_0(E)]}\langle u_{E0}|r|u_i\rangle$$
$$- 2e^{i[\sigma_2(E)+\delta_2(E)]}\langle u_{E2}|r|u_i\rangle\}. \quad (10)$$

By taking the first derivative of the dipole phase with respect to energy, the so-called Wigner-type time delay can be obtained:

$$\tau^W(E) = \frac{d}{dE}\arg[d(E)]. \quad (11)$$

The original Wigner delay is recovered for a short-range potential problem and if there is only one partial wave for the photoelectron.

We comment that the expressions for the transition dipoles given in Eqs. (9) and (10) are valid only for treating atoms in the single-electron model. In many-electron formulations with the inclusion of electron correlation, the expressions for the transition dipole are more complicated, especially when the so-called interchannel couplings are included. In the case of coupling between two channels, the transition dipole, for example, may take the form of Eq. (9) in [25]. Even with the additional complexity, however, the transition dipole for a well-defined continuum photoelectron in a given direction can always be expressed by its dipole amplitude and dipole phase. The latter is the quantity that we try to extract from a streaking experiment. Note that in this work our retrieval methods are based on the SFA model, Eq. (1), where the interactions between the photoelectron and the core within the laser field are not included. Therefore the time delay retrieved from a real experimental spectrogram may differ from the Wigner delay given in Eq. (11), if Eq. (1) does not describe the spectrogram accurately. This happens for XUV generated low-energy photoelectrons in general and is addressed in Sec. V.

In order to apply the FROG algorithm to the streaking spectrogram, additional assumptions beyond Eq. (1) are needed. First, if the exponential term $e^{-i\varphi(p,t)}$ oscillates as a function of t with a period much shorter than the optical cycle of the laser field, according to the derivation in Ref. [21], Eq. (1) can be transformed into

$$S(E,\tau) \approx \left| \int_{-\infty}^{\infty} \chi(t-\tau)e^{-i\varphi(p,t)}e^{iEt}dt \right|^2. \quad (12)$$

The function $\chi(t)$ is called the "temporal electron wave packet," which describes the XUV photoionization process. $\chi(t)$ is related to the energy-domain wave packet $\tilde{\chi}(E)$ by an inverse Fourier transform:

$$\chi(t) = \frac{1}{2\pi}\int_{0}^{\infty}\tilde{\chi}(E)e^{-iEt}dE. \quad (13)$$

First-order perturbation theory of XUV photoionization predicts

$$\tilde{\chi}(E) = \tilde{E}_{\text{XUV}}(\Omega)d(E). \tag{14}$$

Here $\Omega = E + I_p$ denotes the XUV photon energy. $\tilde{E}_{\text{XUV}}(\Omega)$ is the frequency spectrum of the XUV pulse,

$$\tilde{E}_{\text{XUV}}(\Omega) = \int_{-\infty}^{\infty} E_{\text{XUV}}(t)e^{i\Omega t}dt; \tag{15}$$

$d(E)$ is the single-photon transition dipole discussed before. It is actually the same quantity as the $d(p + A(t))$ that appears in Eq. (1), except that in $d(p + A(t))$ the input variable has the units of momentum rather than energy. Second, if one assumes that $\varphi(p,t)$ depends on p weakly such that p in $\varphi(p,t)$ can be replaced by p_0, with p_0 being the center of the momentum of photoelectrons, then Eq. (12) takes the form

$$S(E,\tau) \approx \left| \int_{-\infty}^{\infty} \chi(t - \tau)G(t)e^{iEt}dt \right|^2, \tag{16}$$

with the "gate" function $G(t) = e^{-i\varphi(p_0,t)}$. After taking this "central momentum approximation," Eq. (16) fits the mathematical structure of the FROG equation. Various iterative algorithms can be used to extract $\chi(t)$ and $G(t)$ from $S(E,\tau)$ simultaneously [26,27]. Such methods are usually called FROG-CRAB [20]. In this work we choose to use the FROG algorithm based on the LSGPA [27] because it can avoid interpolation of the spectrogram along the delay axis and therefore it is more suitable for accurately retrieving attosecond wave packets. After $G(t)$ has been extracted, a vector potential, $A(t)$, of the IR field can be calculated from Eq. (2) provided p_0 is given. If the complex atomic dipole $d(E)$ is well known, the XUV pulse $E_{\text{XUV}}(t)$ can be deduced from the extracted wave packet $\chi(t)$ according to Eq. (14). A drawback of the FROG-CRAB method is that it cannot determine the absolute time t; in other words, the output of the FROG algorithm could be $\chi(t - t_0)$ and $G(t - t_0)$, where t_0 is arbitrary. Equivalently, such uncertainty would add a linear term Ωt_0 to the spectral phase of the wave packet $\arg\tilde{\chi}(\Omega)$.

The time delay has also been extracted from the photoelectron spectrogram obtained by solving the TDSE in IR-dressed XUV photoionization processes [14]. The time delay thus extracted depends on the phase of the electron wave packet generated by the combined XUV and IR fields. Compared to the time delay for the electron wave packet generated by the XUV alone, an IR-induced part called the Coulomb-laser coupling (CLC) delay [4] has been identified. While this was carried out theoretically based on the assumption that the XUV and IR pulses are well specified, experimentally this may not be true. In particular, the XUV pulse generated from a high-order harmonic source would contain some chirp. Unless the XUV phase is also retrieved, the method would not be applicable to the analysis of experimental data.

III. RETRIEVING TIME DELAYS USING THE FROG-CRAB METHOD

A. Time delay between the ionization from $2p$ and that from $2s$ subshells of Ne

The Ne atom has two ionization channels from $2p$ and $2s$ subshells, with ionization potentials of 21.56 and 48.47 eV, respectively. The $2p$ and $2s$ photoelectrons are generated simultaneously in an XUV and an IR field. The total electron spectrogram can be expressed by

$$\begin{aligned} S(E,\tau) &\approx \left| \int_{-\infty}^{\infty} [\chi_{2p}(t - \tau) + \chi_{2s}(t - \tau)]e^{-i\varphi(p,t)}e^{iEt}dt \right|^2 \\ &\approx \left| \int_{-\infty}^{\infty} \chi(t - \tau)e^{-i\varphi(p_0,t)}e^{iEt}dt \right|^2. \end{aligned} \tag{17}$$

Here we introduce the total wave packet $\chi(t) = \chi_{2p}(t) + \chi_{2s}(t)$ as the sum of the $2p$ and $2s$ wave packets. By applying FROG-CRAB to the total spectrogram $S(E,\tau)$, $\chi(t)$ can be retrieved. If $S_{2p}(E,\tau)$ and $S_{2s}(E,\tau)$ are well separated in energy, it is possible to distinguish $\tilde{\chi}_{2p}(E)$ and $\tilde{\chi}_{2s}(E)$ from $\tilde{\chi}(E)$. Then one can take the difference between the phases of these two wave packets at the same XUV photon energy Ω, according to Eq. (14),

$$\arg[\tilde{\chi}_{2p}(\Omega)] - \arg[\tilde{\chi}_{2s}(\Omega)] = \arg[d_{2p}(\Omega)] - \arg[d_{2s}(\Omega)]. \tag{18}$$

In this way the dipole phase difference between $2p$ and $2s$ channels can be obtained by canceling the XUV spectral phase. The Wigner time delay between $2p$ and $2s$ ionization $\Delta\tau_{2p(2s)}^W$ is then calculated by taking the energy derivative of this phase difference. Note that if one applies the FROG algorithm to the $2p$ and $2s$ spectrograms individually, the same temporal axis for the two extracted wave packets cannot be guaranteed, thus the obtained time delay is uncertain.

Because retrieval by FROG-CRAB is an iterative process we need to test its accuracy. Here we start with the most favorable conditions. We use the SFA model, Eq. (1), to simulate spectrograms of Ne atom. We first use an 190-as transform-limited XUV pulse. In the energy domain it is centered at $\Omega_0 = 105$ eV, with an FWHM (full width at half-maximum) bandwidth $\Delta\Omega = 9$ eV. Its peak intensity is 8×10^{11} W/cm^2. The IR field is 800 nm in wavelength, has a cosine-squared envelope, and is 6.2 fs in FWHM duration, 10^{12} W/cm^2 in peak intensity, and $0°$ in carrier-envelope phase. The simulated spectrogram is shown in Fig. 1(a). We also use a 280-as chirped XUV pulse which has the same spectral amplitude as the transform-limited pulse but a quadratic spectral phase such that its group delay dispersion (GDD) is 0.0147 fs^2. Figure 1(b) is the spectrogram generated by this chirped XUV. Numerically the input spectrograms are formed by 501×301 matrices with energy step $dE = 0.2$ eV and delay step $d\tau = 0.053$ fs. The input amplitude and phase of the transition dipole matrix elements from $2p$ and $2s$ are plotted in Figs. 1(c) and 1(d).

The phase of the retrieved $2p$ and $2s$ photoelectron wave packets as functions of the photon energy Ω are plotted in Fig. 2 for the cases of transform-limited XUV [Fig. 2(a)] and chirped XUV [Fig. 2(b)]. The retrieved results come from FROG-CRAB using the LSGPA after 100 000 iterations,
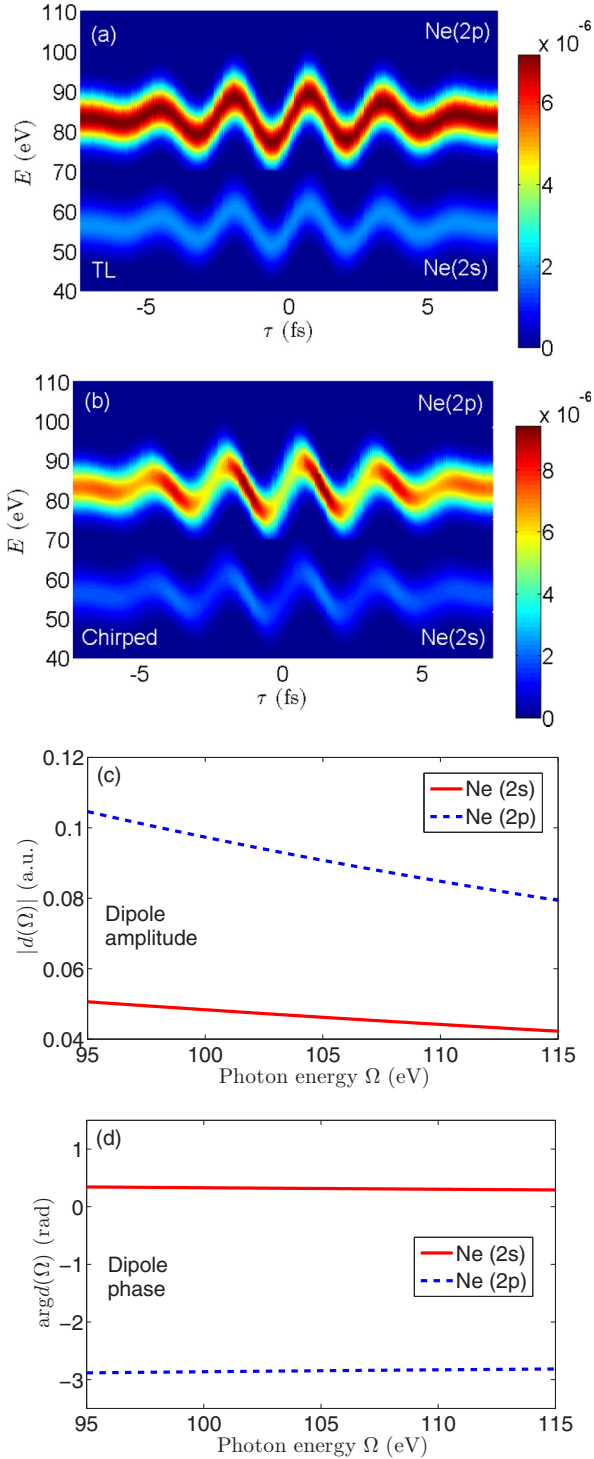
FIG. 1. (a) SFA-simulated Ne spectrogram for a 190-as transform-limited (TL) XUV pulse. (b) Spectrogram for a 280-as chirped XUV. In these simulations the peak of the XUV envelope and the peak of the IR field overlap at $\tau = 0$. A negative τ means that the XUV comes before the IR. (c) Input dipole amplitude and (d) dipole phase for Ne $2p$ and $2s$ ionization channels, calculated using the SAE model potential given in Ref. [23].

where the RMS (root mean square) deviation between the input and the retrieved spectrograms as well as the retrieved wave packet is observed to converge. In the LSGPA we choose
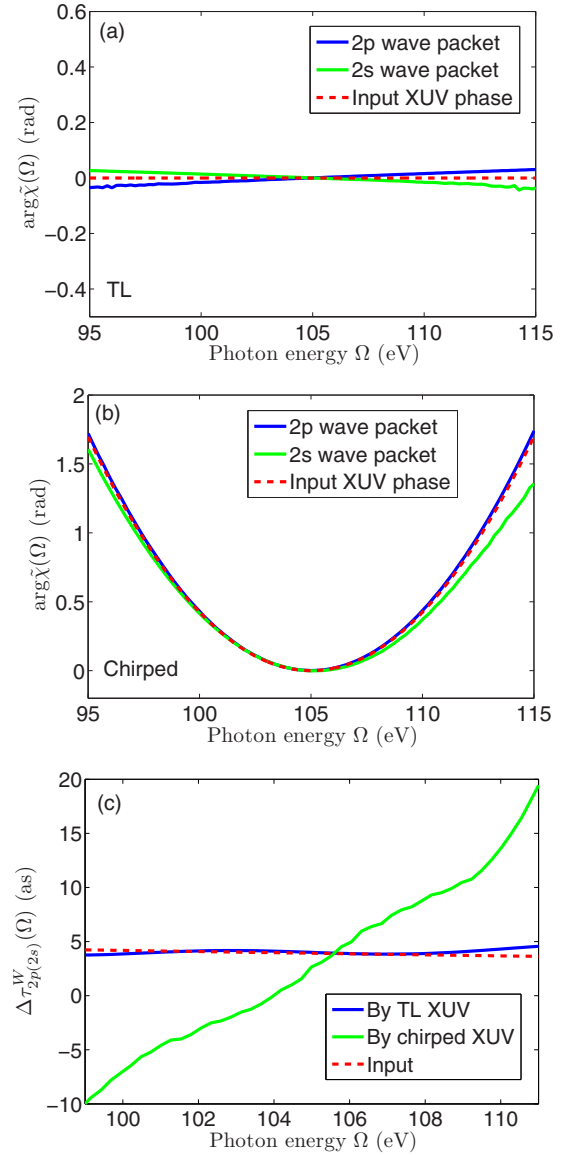
FIG. 2. (a) FROG-CRAB retrieved spectral phases of the $2p$ and $2s$ wave packets for the case of the transform-limited (TL) XUV, compared with the input XUV phase. (b) Retrieved wave-packet phases for the case of the chirped XUV. (c) Retrieved Wigner delay difference $\Delta\tau_{2p(2s)}^{W}$ for both cases compared with the input data. In the energy domain both XUV pulses are centered at 105 eV, with an FWHM bandwidth of 9 eV.

the time step $\delta t = 4.85$ as, so there are $L = 11$ time samples in one delay step $d\tau$. The number of time samples N_t in the retrieved $\chi(t)$ has to be the same as the number of energy samples N_E, and here we choose $N_E = 4096$. According to the discrete Fourier transform relation $\delta E \delta t = 2\pi/N_E$, the input spectrogram has to be readjusted and interpolated along the the energy axis such that the energy step becomes $\delta E = 0.208$ eV and the total energy range becomes $\delta E \times N_E = 853$ eV. For the transform-limited case the retrieved wave-packet phases differ slightly from the input XUV phase, which indicates the effect of the transition dipoles. For the chirped case the XUV phase is much larger than the dipole phase. We can see that the retrieved phase of the $2s$ wave packet has a prominent error

such that it does not follow Eq.(14) accurately. The Wigner time delays between 2p and 2s ionization $\Delta\tau^W_{2p(2s)}$ obtained in both cases are shown in Fig. 2(c) compared with the input value. The retrieved time delays agree very well with the input value for the transform-limited XUV pulse. However, for the chirped pulse, the retrieved time delays vary significantly with the photon energy, from -8 to $+18$ as within the spectral range of the XUV pulse, compared to the expected constant from the input over this spectral range. The large variation of the retrieved time delays over the spectral region also makes a single averaged time delay meaningless. In Eq. (18) it was assumed that the retrieved wave packets follow Eq. (14) exactly. Otherwise, the error will be added to the retrieved dipole phase difference and time delay, as demonstrated by the example here using chirped XUV. We note that the spectrogram in Fig. 2 A of Schultze *et al.* [9] appears to be generated from a chirped XUV pulse, since it is more similar to the spectrogram in Fig. 1(b) than to that in Fig. 1(a). Thus the retrieved 21-as time delay might include error due to the chirp of their XUV pulse. In general, one expected XUV pulse obtained from harmonic generation is chirped. For attosecond pulse trains, see López-Martens *et al.* [28].

B. Time delay between Ar and Ne ionization

In a recent experiment [11], Sabbar *et al.* carried out streaking experiments on mixed Ar and Ne under the same XUV and IR fields. The photoelectrons are obtained in coincidence with the target ions, thus two spectrograms, $S_{Ar}(E,\tau)$ and $S_{Ne}(E,\tau)$, ionized from Ar(3p) and Ne(2p), respectively, can be separated. Since running FROG-CRAB individually cannot guarantee the same temporal axis for the two extracted wave packets, Sabbar *et al.* [11] patched the two spectrograms together by shifting one of them upward along the energy axis. Then, similarly to the Ne 2p (2s) case, FROG was used to analyze the combined spectrogram. Since they are ionized by the same XUV, $S_{Ne}(E,\tau)$ and $S_{Ar}(E,\tau)$ usually share the same energy region. We then shift S_{Ar} by an energy E_{shift} so that the two spectrograms become energetically separate. The combined spectrogram is expressed as

$$S(E,\tau) = S_{Ne}(E,\tau) + S_{Ar}(E - E_{shift}, \tau)$$

$$\approx \left| \int_{-\infty}^{\infty} \chi_{Ne}(t-\tau)e^{-i\varphi(p,t)}e^{iEt}dt \right|^2$$

$$+ \left| \int_{-\infty}^{\infty} \chi_{Ar}(t-\tau)e^{-i\varphi(\sqrt{p^2-2E_{shift}},t)}e^{i(E-E_{shift})t}dt \right|^2.$$

$$(19)$$

In the low-energy part $S_{Ne}(E,\tau)$, p is the momentum of the photoelectrons coming from Ne targets so we can denote $p_{Ne} = p$. In the high-energy part $S_{Ar}(E - E_{shift}, \tau)$, $p = \sqrt{2E}$ corresponds to the energy after shifting upward, while $p_{Ar} = \sqrt{p^2 - 2E_{shift}}$ is the right momentum of the photoelectrons coming from Ar targets. The ranges of the momentum distributions for p_{Ne} and p_{Ar} are similar, thus we can approximate the two terms $e^{-i\varphi(p_{Ne},t)}$ and $e^{-i\varphi(p_{Ar},t)}$ in Eq. (19) by a single term, $e^{-i\varphi(p_0,t)}$, with p_0 being the central momentum. Suppose that $S_{Ne}(E,\tau)$ and $S_{Ar}(E - E_{shift}, \tau)$ do

not overlap; then we have

$$S(E,\tau) \approx \left| \int_{-\infty}^{\infty} \chi(t-\tau)e^{-i\varphi(p_0,t)}e^{iEt}dt \right|^2. \quad (20)$$

The total wave packet $\chi(t) = \chi_{Ne}(t) + \chi_{Ar}(t)e^{-iE_{shift}t}$ can be extracted by applying FROG-CRAB to this combined spectrogram. Therefore one can distinguish $\tilde{\chi}_{Ne}(E)$ and $\tilde{\chi}_{Ar}(E - E_{shift})$ as long as E_{shift} is large enough to make them separate. By comparing the Ar and Ne wave packets at the same photon energy Ω, one can then obtain the dipole phase difference and time delay between Ar and Ne ionization. The error of the time delay retrieved in this way is due to the central momentum approximation. The accuracy of this approximation depends on the range of p_{Ne} or p_{Ar} in which the electron flux is significantly intense. We can roughly estimate the range of momentum $\Delta p \approx \frac{\Delta\Omega}{p_0} + 2A_{max}$, where $\Delta\Omega$ is the bandwidth of the XUV pulse, A_{max} is the maximum value of the vector potential of the laser field, and the central momentum p_0 is determined by the central frequency Ω_0 of the XUV. As $\Delta\Omega$ increases while Ω_0 is fixed, the central momentum approximation will get worse. On the other hand, given the same $\Delta\Omega$, the central momentum approximation will work better if Ω_0 increases.

To test the accuracy of time delay retrieval by patching two spectrograms together, we simulate Ar and Ne spectrograms using Eq. (1), combine them by shifting the Ar spectrogram, and then use FROG-CRAB to analyze the entire spectrogram. Figure 3(a) is the spectrogram generated using a transform-limited XUV pulse of 160-as duration (FWHM bandwidth $\Delta\Omega = 11.5$ eV), and Fig. 3(b) is generated with a transform-limited XUV pulse of 80-as duration ($\Delta\Omega = 23$ eV). Both XUV pulses are centered at 60 eV and have a peak intensity of 10^{12} W/cm^2. The IR field is 800 nm in wavelength, has a cosine-squared envelope, is 8.8 fs in FWHM duration, and is 10^{12} W/cm^2 in peak intensity. In Figs. 3(a) and 3(b) the Ar spectrogram has been multiplied by a factor of 10 and then shifted upward by 60 eV. Numerically both spectrograms are formed by 700×441 matrices with energy step $dE = 0.2$ eV and delay step $d\tau = 0.053$ fs. Figures 3(c) and 3(d) show the input transition dipole amplitude and phase for Ar and Ne, based on the SAE model potential given in Ref. [23]. For Ar this potential predicts a Cooper minimum [29] near 42 eV in photon energy.

We apply LSGPA FROG-CRAB to these spectrograms with the parameters $\delta t = 1.98$ as, $L = 27$, $N_E = 4096$, and $\delta E = 0.511$ eV. The input spectrograms have been readjusted and interpolated along the energy axis. After 100 000 iterations the FROG algorithm is verified to achieve converged results. Furthermore, we change the energy shift E_{shift} to generate new input spectrograms and repeat the FROG-CRAB with the parameters $dE, d\tau$, and $\delta t, N_E, \delta E$ fixed. Figure 4(a) shows the retrieved time delay $\Delta\tau^W_{Ar(Ne)}$ using the 160-as XUV compared with the input value. Since the XUV has a relatively narrow bandwidth, for $E_{shift} \geqslant 50$ eV the Ne and Ar spectrograms can be well separated, and the central momentum approximation works quite well. The retrieved time delay is not sensitive to E_{shift} and the error is less than 10 as within the FWHM bandwidth of the XUV. However, for the case of the 80-as broadband XUV, the retrieved results strongly depend on E_{shift},
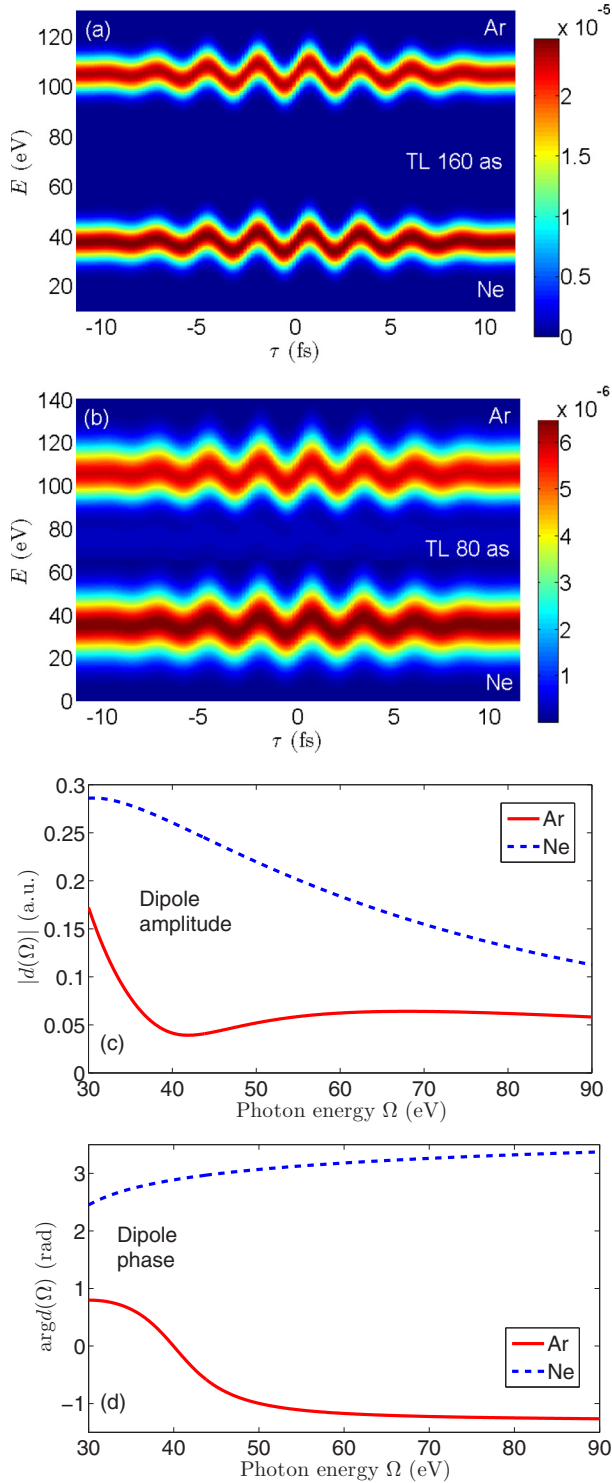
FIG. 3. (a) SFA simulated spectrogram of Ar and Ne using a transform-limited (TL) 160-as XUV pulse. (b) Simulated spectrogram using a 80-as XUV pulse. In both cases the Ar spectrogram has been multiplied by a factor of 10 and shifted upward by 60 eV. (c) Input dipole amplitude and (d) dipole phase for Ar($3p$) and Ne($2p$) ionization, calculated using the SAE model given in Ref. [23].

as shown in Fig. 4(b). When E_{shift} takes a value of 50 or 60 eV, it is not large enough to totally separate the Ar and Ne spectrograms, and the retrieved time delay has an error of
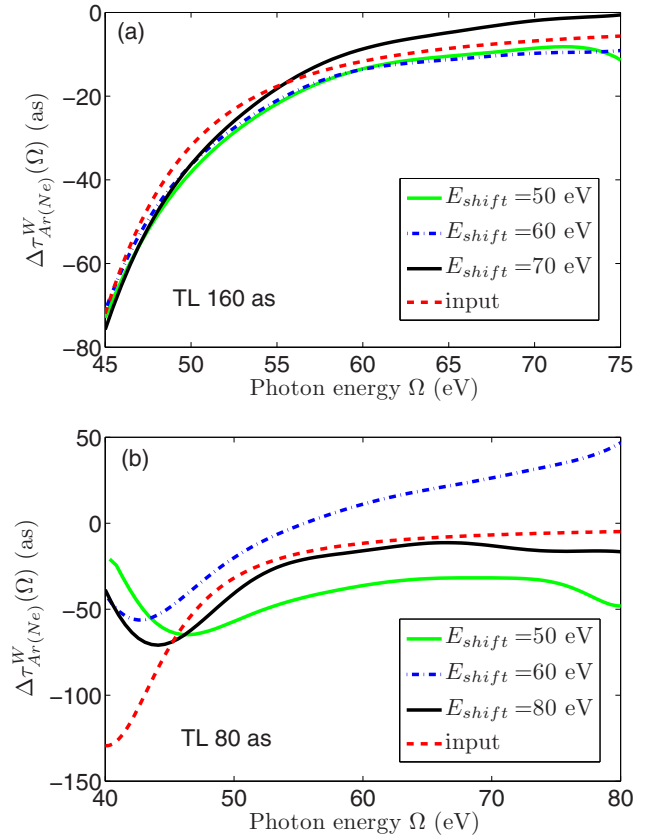
FIG. 4. FROG-CRAB retrieved Wigner time delay between the ionization of Ar and that of Ne $\Delta \tau_{\mathrm{Ar(Ne)}}^{W}$ for various energy shifts E_{shift}, compared with the input value. (a) Using an 160-as transform-limited (TL) XUV, centered at 60 eV, with an FWHM bandwidth of 11.5 eV. (b) Using an 80-as TL XUV, centered at 60 eV, with an FWHM bandwidth of 23 eV.

more than 20 as. When $E_{shift} = 80$ eV, the two spectrograms are well separated, thus the retrieved time delay becomes closer to the input value. The remaining error comes from the central momentum approximation since here we use an XUV pulse with a larger $\Delta \Omega$. In summary, FROG-CRAB-based time delay retrieval by patching two spectrograms together is reliable only for narrow-band XUV pulses, which is the case for the experiment by Sabbar *et al.* [11].

IV. TIME DELAY RETRIEVAL THROUGH A MODIFIED FROG-CRAB FITTING PROCEDURE FOR BROADBAND ATTOSECOND PULSES

We have shown that in order to retrieve the dipole phase difference or time delay successfully using the FROG-CRAB method, the XUV pulse has to have small attochirp and a narrow bandwidth. The accuracy of FROG-CRAB is limited by the central momentum approximation. Here we propose a different approach to improve the accuracy of time delay retrieval when using broadband XUV pulses or more intense IR fields. To be more specific, suppose we have Ar and Ne spectrograms generated under the same XUV and IR field, and we assume that the dipole amplitude and phase of Ne are known and the dipole amplitude of Ar is also known

(from XUV ionization alone); our goal is to retrieve the Ar dipole phase. This can be done in three steps. First, the FROG algorithm is used to extract the electron wave packet $\tilde{\chi}_{Ne}(E)$ from the Ne spectrogram. After dividing this wave packet by the complex transition dipole $d_{Ne}(E)$ we obtain the XUV pulse. Second, we set time 0 at the peak of the XUV envelope and retrieve the IR field by fitting this Ne spectrogram directly using Eq. (1), i.e., without the central momentum approximation. Third, since both XUV and IR have been extracted, we then retrieve the dipole phase of Ar by fitting the Ar spectrogram, again based on Eq. (1).

We use the SFA model, Eq. (1), to simulate both Ar and Ne spectrograms under the same XUV and IR fields, with the one-electron model potentials obtained from Ref. [23]. Figures 5(a) and 5(c) are generated by a transform-limited XUV pulse which is 80 as in FWHM duration and 10^{12} W/cm^2 in peak intensity. In the energy domain the amplitude of this pulse has a Gaussian shape centered at 60 eV with a 23-eV FWHM bandwidth. Figures 5(b) and 5(d) are generated using another 130-as chirped XUV pulse which has the same spectral amplitude as the transform-limited pulse. The spectral phase and temporal envelope of the input chirped pulse are shown in Figs. 6(c) and 6(d), respectively. The IR field is 800 nm in wavelength, has a cosine-squared envelope, and is 8.8 fs in FWHM duration, and we increase its peak intensity to 10^{13} W/cm^2. In the first step we use the FROG-CRAB algorithm to retrieve the XUV pulses from Ne spectrograms [Figs. 5(a) and 5(b)] by taking advantage of the known atomic dipole of Ne. Numerically both spectrograms are discretized into 650×441 matrices with energy step $dE = 0.155$ eV and delay step $d\tau = 0.053$ fs. In FROG-CRAB we use the parameters $\delta t = 8.89$ as, $L = 6$, $N_E = 2048$, and $\delta E = 0.227$ eV. The retrieved XUV phase and temporal envelope after 100 000 iterations compared with the input XUV for the transform-limited case are plotted in Figs. 6(a) and 6(b), and those for the chirped case, in Figs. 6(c) and 6(d). We have set $t = 0$ at the peak of the XUV envelope. Both the 80-as transform-limited and the 130-as chirped XUV pulses can be successfully retrieved. The central momentum approximation used in FROG-CRAB leads to the remaining errors, especially to the errors in the satellite pulses shown in Fig. 6(d).

The next step is the retrieval of the IR field from the Ne spectrogram using the known Ne dipole and the extracted XUV. The IR field is obtained by fitting the spectrogram directly according to Eq. (1). Here we choose to use the micro-GA (genetic algorithm) [30] with the fitness function given by

$$Q = \iint (\sqrt{S_{input}(E,\tau)} - \beta\sqrt{S_{fitting}(E,\tau)})^2 dE d\tau, \quad (21)$$

where β is an overall renormalizing factor treated as a fitting parameter. In order to speed up the GA optimization, the spectrograms $S_{input}(E,\tau)$ and $S_{fitting}(E,\tau)$ are discretized into 47×441 matrices with energy step $dE = 2.24$ eV and delay step $d\tau = 0.053$ fs. We model the IR field as

$$E_{IR}(t) = f(t)\cos[\omega_L(t - \Delta)]. \quad (22)$$

The envelope $f(t)$ is constructed by a set of samples (t_i, f_i) through cubic-spline interpolation. Since the envelope is a smooth function, only seven samples are used here. The
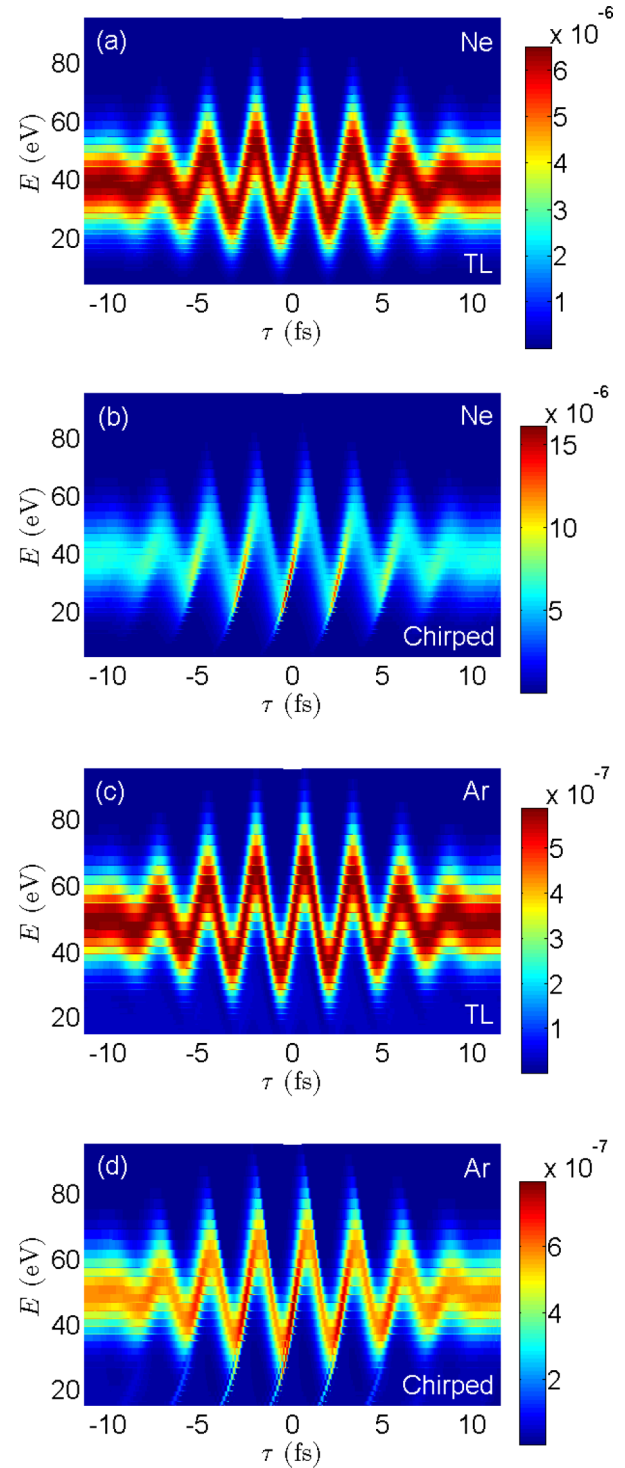
FIG. 5. SFA simulated spectrograms: (a) Ne target, 80-as transform-limited (TL) XUV; (b) Ne target, 130-as chirped XUV; (c) Ar target, 80-as TL XUV; (d) Ar target, 130-as chirped XUV.

horizontal coordinates t_i are fixed, while the vertical coordinates f_i as well as ω_L and Δ are set as fitting parameters. Then the micro-GA is applied to optimize these parameters. There are five individuals in each generation and the retrieved results are obtained after 1000 generations, where we confirm the convergence. Figure 7 shows the retrieved IR field by this
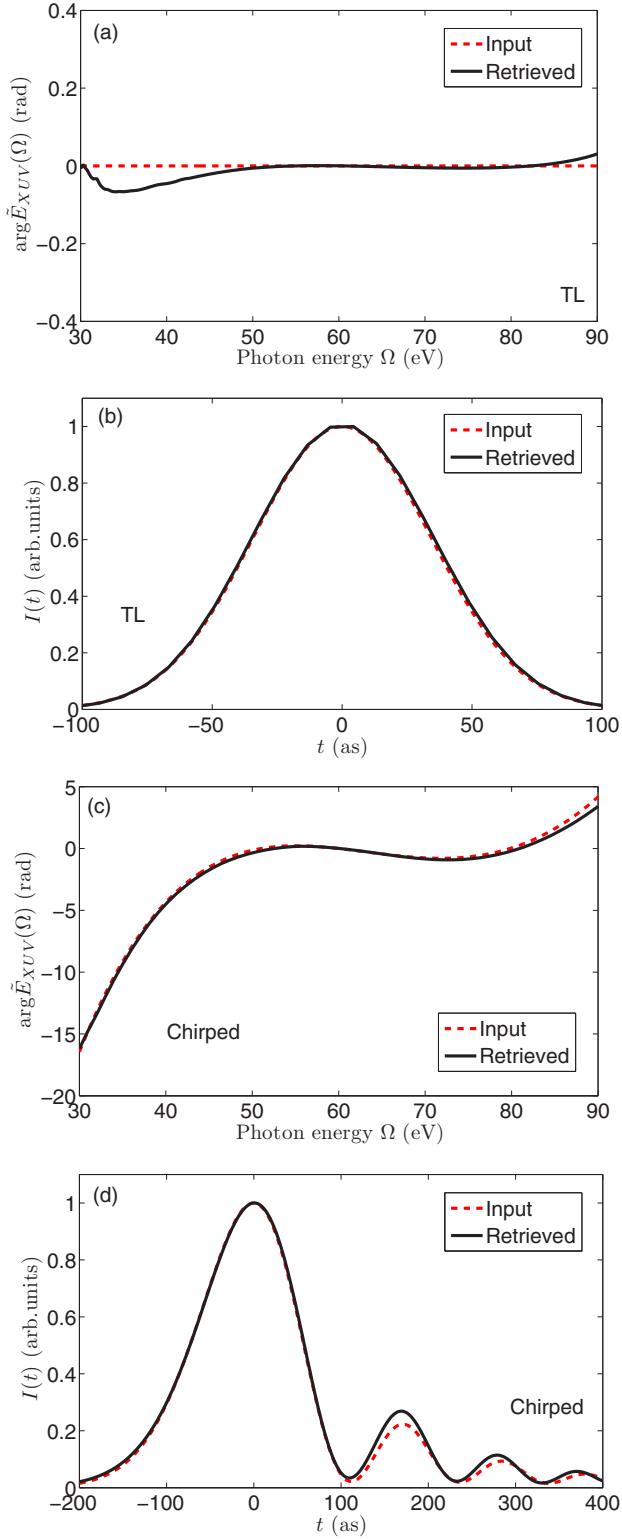
FIG. 6. (a) Retrieved XUV spectral phase and (b) retrieved XUV temporal envelope compared with the input value, for the case of the transform-limited XUV. (c, d) Similar plots, but for the case of the chirped XUV. XUV pulses are extracted from Ne spectrograms using FROG-CRAB.

fitting method compared with the input IR for the case of transform-limited XUV. We also plot the output IR field from the FROG-CRAB algorithm as the dot-dashed line. Although
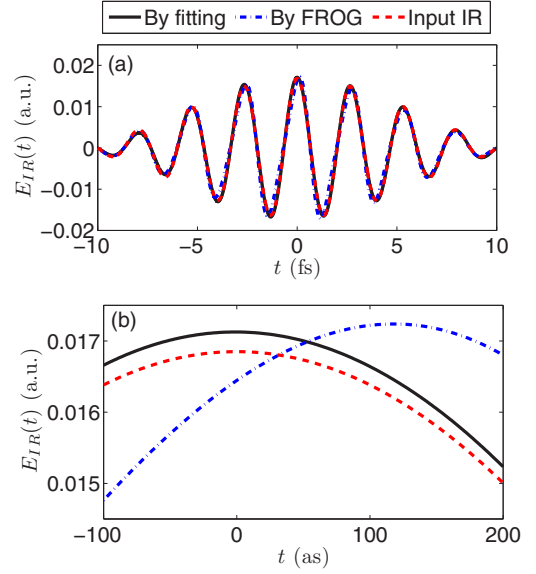
FIG. 7. Retrieved IR field from the Ne spectrogram with transform-limited XUV. (a) Solid black line: retrieved IR through direct fitting. Dot-dashed blue line: output IR field from FROG-CRAB by setting $p_0 = 1.68$. Dashed red line: input IR field. (b) Zoomed-in plot of (a) near $t = 0$.

the one from FROG-CRAB appears to be in good agreement with the input IR in Fig. 7(a), the agreement on the attosecond time scale shows its deficiency [see Fig. 7(b)]; the IR peak position was off by more than 100 as. Here we can compare IR peak positions because $t = 0$ has been determined by the XUV field. In comparison, the IR field extracted by direct fitting is off by only about 2 as, and this IR field will be used to extract the dipole phase of Ar. For the case of the chirped XUV, the IR field was accurately retrieved by this fitting process too.

The last step is using fitting to extract the dipole phase or Wigner delay of Ar from the Ar spectrogram without the central momentum approximation. The dipole phase $\arg d(E)$ is constructed with samples $(E_i, \arg d_i)$ through cubic-spline interpolation. In this case 12 samples are used and the optimal vertical coordinates $\arg d_i$ are obtained by micro-GA. During this optimization the horizontal coordinates E_i are fixed, but they are not evenly distributed. We put more samples on the low-energy side and fewer on the high-energy side since the dipole phase should change slowly in the high-energy region. There are eight individuals in each generation and the results are obtained after 2000 generations. The retrieved Wigner delay of Ar by fitting for both the transform-limited and the chirped XUV cases are plotted in Fig. 8. The input τ_{Ar}^W within the FWHM bandwidth of the XUV pulse is accurately retrieved by this fitting method for the case of transform-limited XUV, while errors of up to 10 as are observed if the chirped XUV is used. In Sec. III B we have retrieved the delay difference $\Delta\tau_{Ar(Ne)}^W = \tau_{Ar}^W - \tau_{Ne}^W$ by using FROG-CRAB for the case of an 80-as transform-limited XUV pulse [see Fig. 4(b)]. We choose the $\Delta\tau_{Ar(Ne)}^W$ obtained by setting $E_{shift} = 80$ eV and add the τ_{Ne}^W which is calculated from the input Ne dipole to it; then we can get a τ_{Ar}^W retrieved by the FROG-CRAB method. This result is also plotted in Fig. 8 by the dot-dashed line, to be compared with the fitting result (solid blue line). Clearly
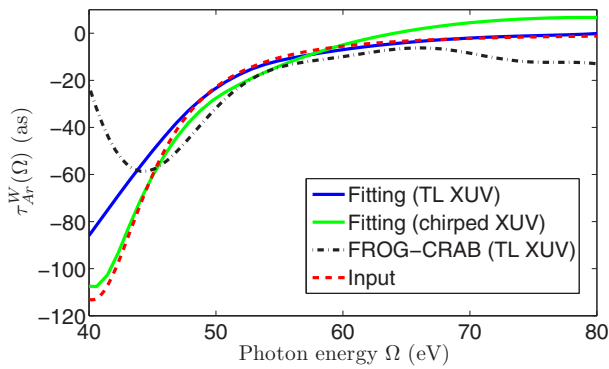
FIG. 8. Wigner delay of Ar. Solid blue line: retrieved by fitting for the case of 80-as transform-limited (TL) XUV. Solid green line: retrieved by fitting for the case of 130-as chirped XUV. Dot-dashed black line: retrieved from FROG-CRAB in Sec. III B for the case of 80-as TL XUV, by choosing $E_{shift} = 80$ eV and using the input Ne dipole. Dashed red line: input data. In the energy domain the XUV pulses are centered at 60 eV, with an FWHM bandwidth of 23 eV.

the fitting approach is more accurate because it gets rid of the central momentum approximation in its second and third steps. However, since the central momentum approximation is still included in the first step in our procedure, the errors in the extracted XUV pulses will affect the accuracy of the retrieved time delay. This effect becomes more prominent when chirped XUV pulses are used.

In Fig. 5 we can see that the XUV phase has a strong effect on the spectrogram. However, the spectrogram is not very sensitive to the dipole phase of the target. To demonstrate this point, we use two artificial targets which have different dipole phases from the input Ar target and generate spectrograms under the same 80-as transform-limited XUV and the same IR field. Figure 9(a) shows the corresponding Wigner delays of the two artificial targets as well as that of the input Ar. Figures 9(b) and 9(c) are their electron spectra at two particular delays between the XUV and the IR. Although the Wigner delays can differ by more than 20 as, the electron spectrograms or their sectional plots at fixed delays are not visually different. This insensitivity of the streaked electron spectra with respect to the dipole phase makes it challenging to retrieve the accurate dipole phase, especially when the XUV phase has large attochirp so that the effect of the dipole phase becomes more insignificant.

To test the robustness of our approach with respect to noise, we repeat the procedure above for spectrograms contaminated by random errors. Starting from the Ne and Ar spectrograms [Figs. 5(a) and 5(c)], we add random noise and treat the new spectrograms as the input of our retrieval. Here the noise at each data point has a mean-zero normal distribution with a standard deviation of 5% or 10% of the original value. Figure 10 demonstrates that this modified FROG-CRAB fitting method is stable for random errors up to 10%, and therefore it can actually be applied to real experimental data.

Furthermore, our retrieval method relies on the knowledge of the Ne dipole. Since the dipole phase of Ne is not experimentally accessible with any static measurement, it can only be calculated theoretically from a certain model potential
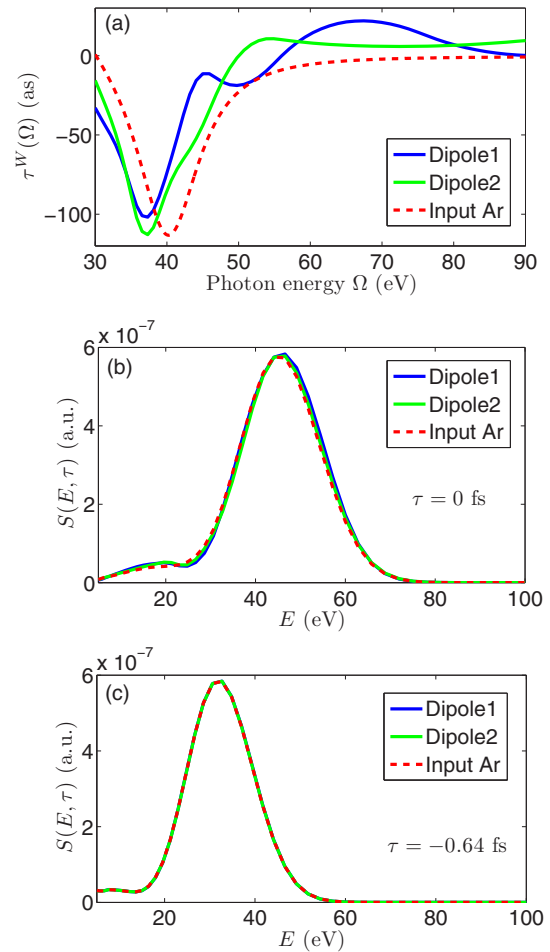
FIG. 9. (a) Wigner delays for the two artificial targets compared with the Wigner delay of the input Ar target. (b) Photoelectron spectra for these targets at $\tau = 0$ fs. (c) Photoelectron spectra at $\tau = -0.64$ fs.

so far. In Fig. 11 we plot the dipole amplitude and phase of Ne as well as its corresponding Wigner delay, calculated from Green's potential [31] and Tong and Lin's potential [23], respectively. One can see that as the photon energy is between 30 and 90 eV the dipole phase given by these two model
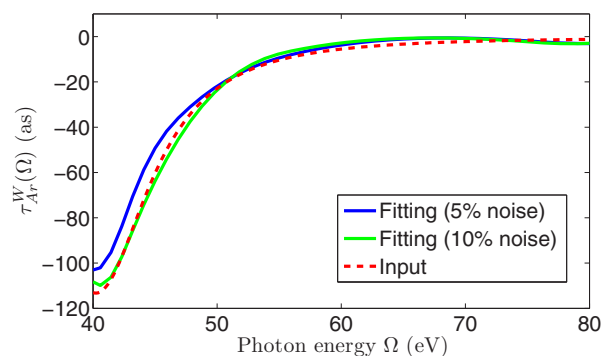
FIG. 10. Wigner delay of Ar retrieved by the fitting approach compared with the input value. We have added 5% or 10% random errors to the original Ne and Ar spectrograms, Figs. 5(a) and 5(c), as the new input data.
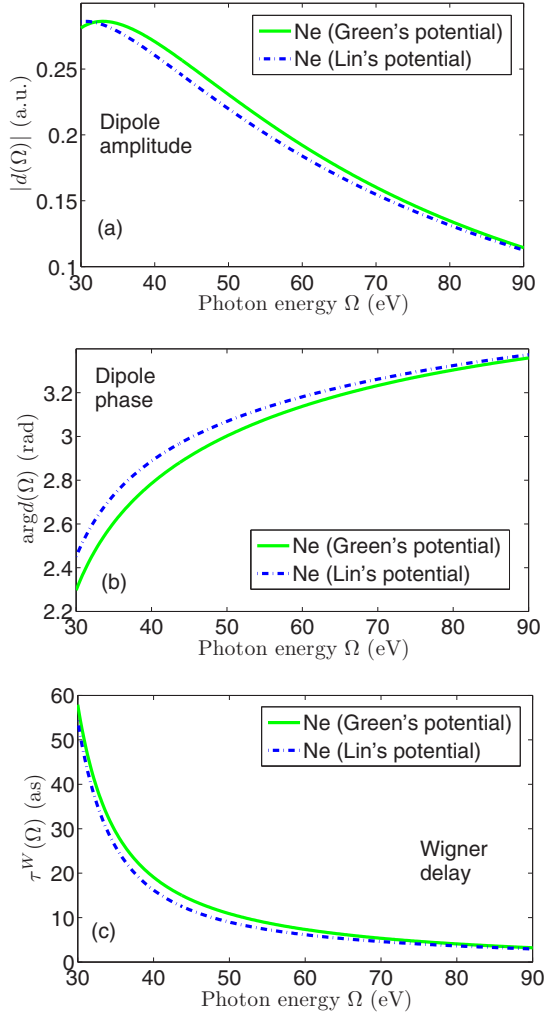
FIG. 11. (a) Dipole amplitude; (b) dipole phase; (c) corresponding Wigner delay of the Ne atom calculated using the SAE model potential given by Green [31] compared with that calculated using Tong and Lin's potential [23].

potentials can differ by 0.1 rad, and the Wigner delay can differ by 3 as.

The Ne and Ar spectrograms in Fig. 5 are generated using Lin's model potential and the retrieval results presented above are based on the Ne dipole which is given by the same model potential. It is necessary to check the sensitivity of our retrieval method with respect to the choice of the model potential of the Ne atom. That is, starting from Figs. 5(a) and 5(c), we repeat the above procedure but use the Ne dipole given by Green's potential. The new retrieval results together with the old ones using Lin's potential are plotted in Fig. 12. One can see that the XUV or IR fields retrieved by using these two Ne dipoles do not show a visible difference. The retrieved Wigner delay of Ar does not strongly depend on the choice of Ne dipole either. After using Green's potential for the Ne atom the errors in the retrieved Ar time delay within $\Omega = 50$ to 70 eV are below 6 as. Such robustness with respect to the choice of the dipole phase of the reference target again supports the applicability of our modified FROG-CRAB fitting approach.
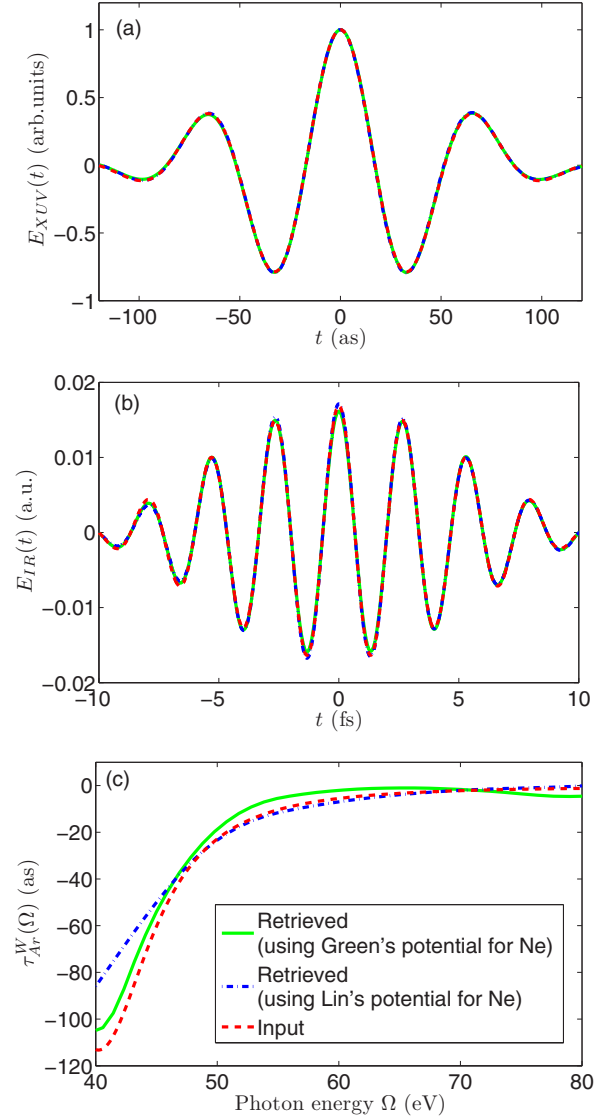
FIG. 12. (a) XUV pulse retrieved by FROG-CRAB. (b) IR field retrieved by the fitting method from the Ne spectrogram [Fig. 5(a)]. (c) Wigner delay of Ar extracted by the fitting method from Fig. 5(c). Solid green line: retrieved using Green's potential for Ne. Dot-dashed blue line: retrieved using Lin's potential for Ne as a comparison. Dashed red line: input values.

V. FROG-CRAB METHOD FOR LOW-ENERGY PHOTOELECTRONS

The retrieval methods presented above assume that the spectrograms can be accurately modeled by the SFA. However, the SFA equation, (1), does not take into account the interaction between the continuum electron and the ionic core. It is a good approximation only for high-energy photoelectrons with energies higher than 30 or 40 eV. In Fig. 13 we compare low-energy spectrograms calculated by using the SFA and by solving the SAE TDSE numerically, for both Ar and Ne targets, with the one-electron model potentials given in Ref. [23]. In the TDSE computation the discrete-variable-representation basis set is used [32,33], and the box size and number of grid points are chosen to ensure convergence. The spectrograms
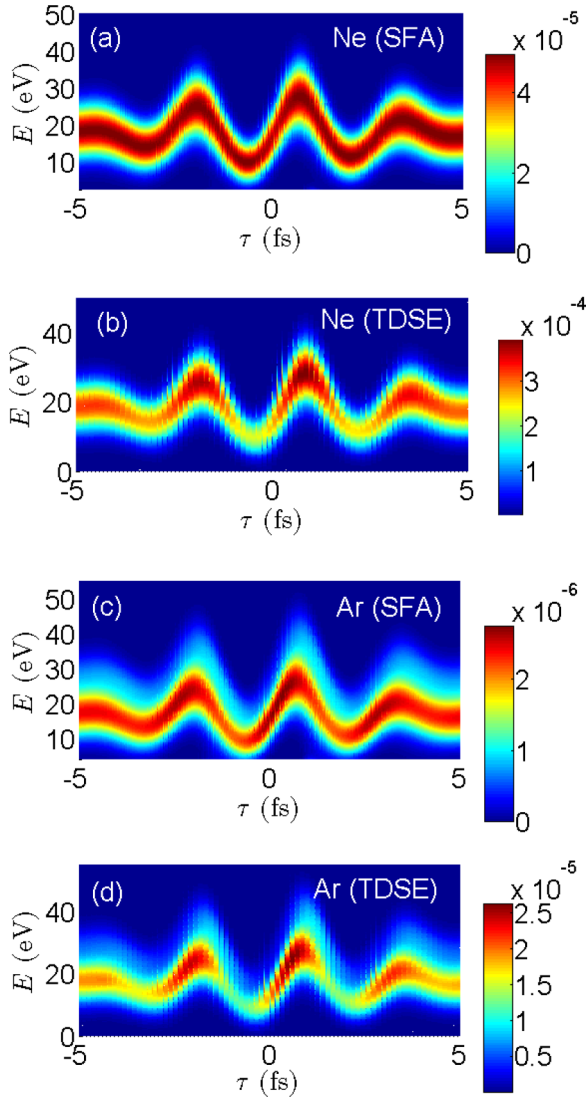
FIG. 13. (a) SFA and (b) TDSE simulated Ne spectrograms. (c) SFA and (d) TDSE simulated Ar spectrograms. A 160-as transform-limited XUV pulse is used, which is centered at 40 eV, with an FWHM bandwidth of 11.5 eV.

in Fig. 13 are generated by a transform-limited XUV pulse which is 160 as in FWHM duration and 10^{12} W/cm^2 in peak intensity. In the energy domain the amplitude of this pulse has a Gaussian shape centered at 40 eV, with an 11.5-eV FWHM bandwidth. The IR field is 800 nm in wavelength, has a cosine-squared envelope, is 4.4 fs in FWHM duration, and is 10^{13} W/cm^2 in peak intensity. Numerically the SFA spectrograms are formed by 440×153 matrices with energy step $dE = 0.136$ eV and delay step $d\tau = 0.067$ fs, while the TDSE spectrograms are formed by 220×77 matrices with energy step $dE = 0.272$ eV and delay step $d\tau = 0.133$ fs in order to reduce the computational load. Clearly one can see the error of the SFA model compared to the TDSE results from these spectrograms.

Similarly to what we did in the first step in Sec. IV, we use the FROG-CRAB to extract the XUV pulses from low-energy Ne spectrograms, but here the input spectrograms
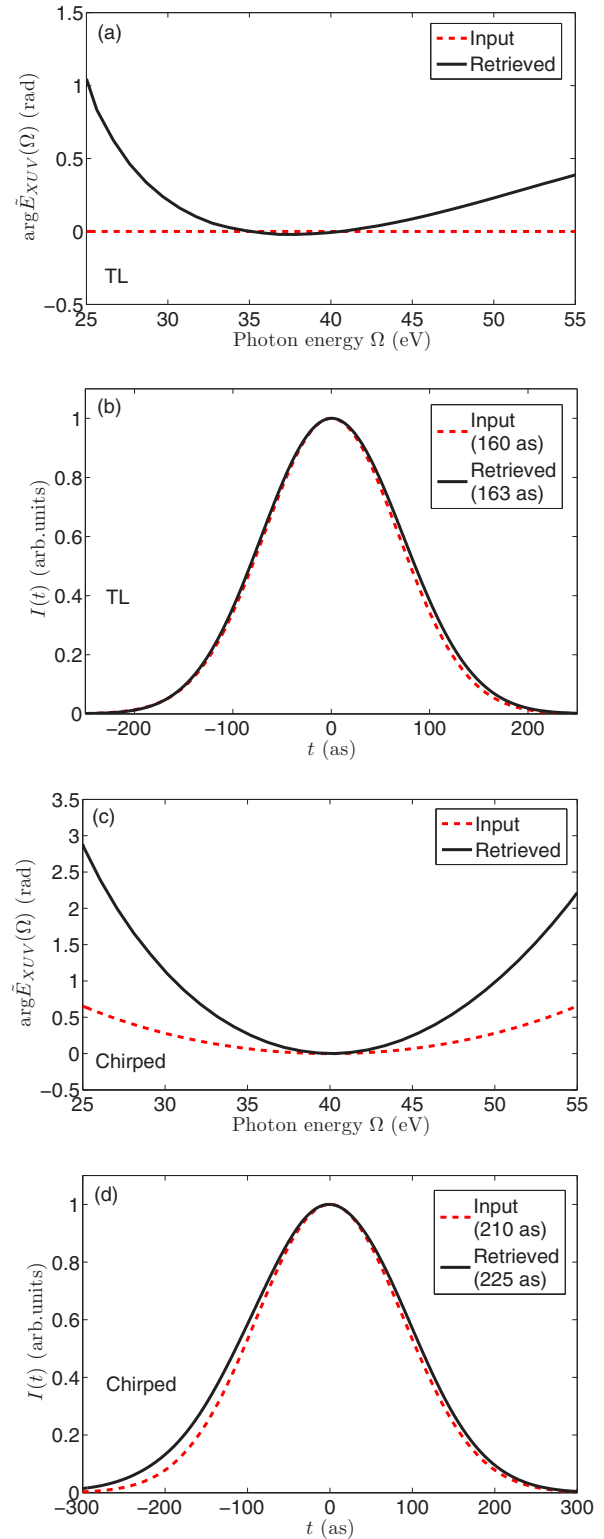
FIG. 14. (a) Retrieved XUV spectral phase and (b) retrieved XUV temporal envelope compared with the input value, for the case of the transform-limited XUV. (c, d) Similar plots, but for the case of the chirped XUV. XUV pulses are extracted from low-energy Ne spectrograms simulated by solving TDSE.

are simulated by solving the TDSE. Figures 14(a) and 14(b) shows the retrieved XUV spectral phase and temporal envelope from the spectrogram [Fig. 13(b)] after 100 000 iterations.

In FROG-CRAB we choose the parameters $\delta t = 0.995$ as, $L = 134$, $N_E = 4096$, and $\delta E = 1.01$ eV. One can see that the retrieved XUV phase has a small chirp; as a result, the retrieved pulse duration is 163 as, compared to the input value of 160 as for this transform-limited pulse. We also use the TDSE to generate a Ne spectrogram with a 210-as chirped XUV pulse which has the same spectral amplitude as the transform-limited pulse but a quadratic phase (GDD $= 0.00735$fs^2). Figures 14(c) and 14(d) show the retrieved XUV pulse from this spectrogram. For this chirped case the FROG-CRAB method has a larger error such that the retrieved pulse duration becomes 225 as, compared to the input value 210 as. These results show that relatively accurate XUV pulses can be retrieved using the FROG-CRAB method even though the SFA model used in the method does not describe the spectrogram very accurately, at least for XUV pulses of the typical attosecond duration (100 to 200 as).

The limitation of the SFA model for low-energy photo-electrons has a more significant effect on the dipole phase or time delay retrieval. Here we patch the TDSE simulated Ne and Ar spectrograms [Figs. 13(b) and 13(d)] together. The Ar spectrogram has been multiplied by a factor of 16 and then shifted upward by 60 eV. FROG-CRAB is then applied to the whole spectrogram and a total electron wave packet is extracted, from which we separate the Ar and Ne wave packets and compare them at the same photon energy. In LSGPA FROG-CRAB we use the parameters $\delta t = 1.99$ as, $L = 67$, $N_E = 4096$, and $\delta E = 0.507$ eV, thus the input spectrograms need to be readjusted along the energy axis. Figures 15(a) and 15(b) show the amplitude and phase of the two extracted wave packets after 100 000 iterations compared with that of the input XUV pulse. One can see that the amplitude of the Ar or Ne photoelectron wave packet differs from the XUV amplitude, which demonstrates the role of the transition dipole amplitude. We then calculate the phase difference between the two electron wave packets and take the derivative of this difference with respect to the energy to obtain the photoionization time delay between Ar and Ne, shown by the solid blue line in Fig. 15(c). The retrieved time delay can only qualitatively reproduce the input Wigner time delay. Within the XUV FWHM bandwidth the error can be up to 50 as, and the minimum in the retrieved result shifts by 2 eV compared with that in the input value. According to the assumption that

$$\tau^{\text{streaking}}(\Omega) = \tau^W(\Omega) + \tau^{\text{CLC}}(\Omega), \qquad (23)$$

where $\tau^{\text{streaking}}$ is the time delay measured in the streaking experiment, τ^W is the Wigner delay, and τ^{CLC} is the CLC delay introduced from earlier theoretical analyses for systems that have a long-range Coulomb potential tail [4,14,18], we can subtract the CLC delay difference $\tau^{\text{CLC}}_{\text{Ar(Ne)}}(\Omega) = \tau^{\text{CLC}}_{\text{Ar}}(\Omega) - \tau^{\text{CLC}}_{\text{Ne}}(\Omega)$ from the FROG-CRAB retrieved time delay between Ar and Ne [see the solid green line in Fig. 15(c)]. Note that $\tau^{\text{CLC}}_{\text{Ar(Ne)}}$ is a positive quantity. After subtracting the CLC part $\Delta\tau^{\text{CLC}}_{\text{Ar(Ne)}}$, the error in the retrieved Wigner delay $\Delta\tau^W_{\text{Ar(Ne)}}$ is reduced but not eliminated. On the contrary, if we combine the two SFA simulated spectrograms [Figs. 13(a) and 13(c)] in the same way as the input of FROG-CRAB, the retrieved time delay agrees with the input value quite well. Therefore the error
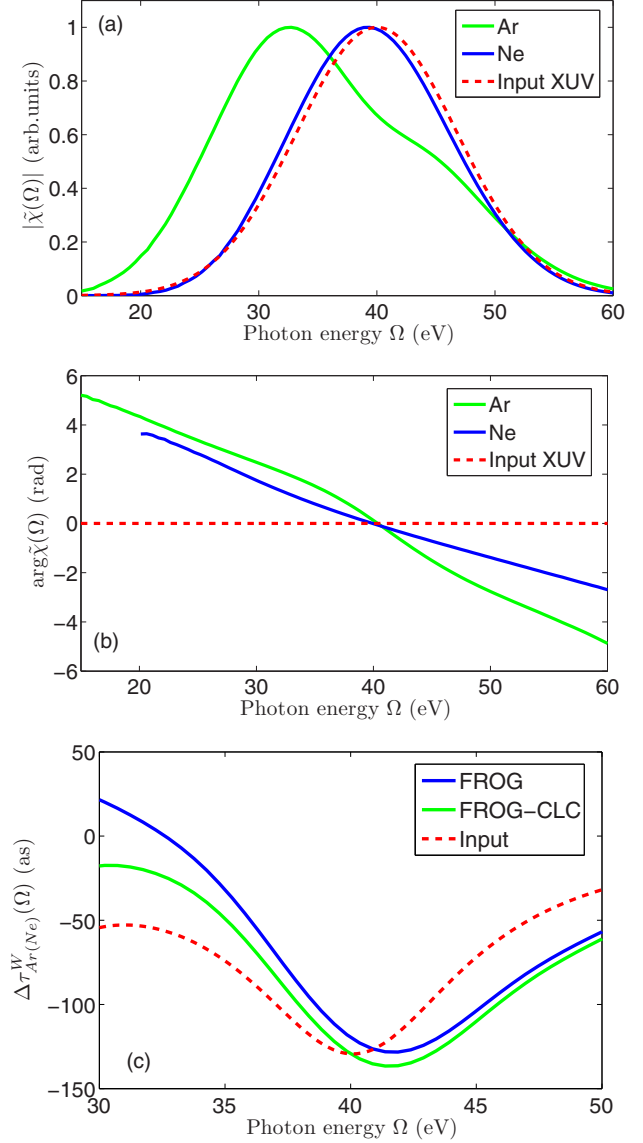
FIG. 15. (a) Amplitude and (b) phase of the retrieved photoelectron wave packets of Ar and Ne as functions of the photon energy Ω, compared with the amplitude and phase of the input XUV pulse. Wave packets are retrieved using FROG-CRAB from combined Ar and Ne spectrograms simulated by TDSE. (c) Time delay between the ionization of Ar and that of Ne. Solid blue line: by taking the energy derivative of the phase difference between the two retrieved wave packets in (b). Solid green line: after subtracting the positive CLC term $\Delta\tau^{\text{CLC}}_{\text{Ar(Ne)}}(\Omega)$. Dashed red line: input Wigner delay between Ar and Ne. The input XUV pulse is transform-limited (TL) with an FWHM duration of 160 as. In the energy domain it is centered at 40 eV, with an FWHM bandwidth of 11.5 eV.

in the retrieved time delay from TDSE simulated spectrograms reflects the deficiency of the SFA model on which the FROG-CRAB method is based.

Additionally, we repeat the micro-GA fitting method presented in Sec. IV for the TDSE simulated spectrograms [Figs. 13(b) and 13(d)]. Note that the XUV spectral phase in Fig. 14(a) is obtained by subtracting the dipole phase of Ne from the phase of the Ne wave packet $\tilde{\chi}_{\text{Ne}}(\Omega)$ extracted
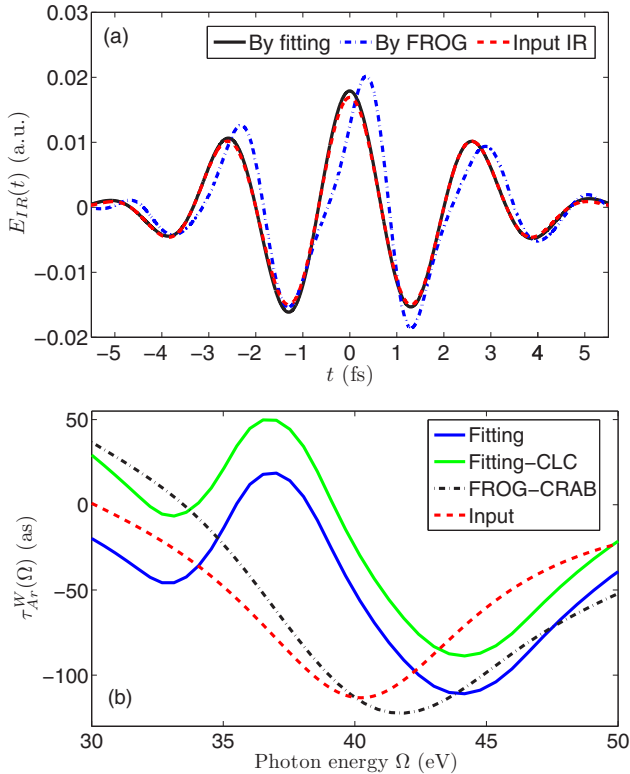
FIG. 16. (a) Retrieved IR field from the Ne spectrogram simulated by TDSE. Solid black line: retrieved IR by fitting. Dot-dashed blue line: output IR field from FROG-CRAB by setting $p_0 = 1.16$. Dashed red line: input IR field. (b) Photoionization time delay of Ar. Solid blue line: retrieved from the Ar spectrogram simulated by TDSE through GA fitting. Solid green line: after subtracting the negative CLC term $\tau_{Ar}^{CLC}(\Omega)$. Dot-dashed black line: retrieved by FROG-CRAB, using the input Ne dipole. Dashed red line: input Wigner delay of Ar.

using FROG-CRAB. We can go further by subtracting an additional phase, $\psi_{Ne}^{CLC}(\Omega)$, of which the CLC delay $\tau_{Ne}^{CLC}(\Omega)$ is the derivative, from the above result; then a new spectral phase of the XUV can be achieved. Unfortunately, the retrieved XUV pulse "corrected" by the CLC term is even less accurate than the one without such correction. The CLC-corrected pulse has a duration of 173 as, compared to the noncorrected 163-as pulse shown in Fig. 14(b). For this reason we choose to use the non-corrected XUV pulse in the retrieval of the IR field as well as the Ar dipole phase. In Fig. 16(a) we can see that the IR field obtained from the Ne spectrogram by FROG-CRAB has considerable errors, whereas the fitting method can successfully reproduce the input IR field. In this fitting approach we use seven samples to construct the IR envelope. There are five individuals in each generation and the result comes after 2000 generations. Since the fitting method is based on the SFA equation, (1), this result shows that the SFA model can be accurate enough for retrieving the IR field. In Fig. 16(b) we plot the photoionization time delay of Ar retrieved from the Ar spectrogram by GA fitting by the solid blue line. In this fitting approach we use the known dipole amplitude of Ar as well as the extracted XUV and IR field, and the dipole phase is discretized into 10 samples. There are eight individuals in each generation and the converged result

comes after 2000 generations. We then subtract the CLC delay $\tau_{Ar}^{CLC}(\Omega)$, which is negative, from the fitting result (see the solid green line). For comparison, we also plot the Wigner delay of Ar retrieved by FROG-CRAB by the dot-dashed black line. This value is obtained by adding the Wigner delay of Ne calculated from the input Ne dipole to the retrieved $\Delta\tau_{Ar(Ne)}^{W}$ by FROG-CRAB [solid green line in Fig. 15(c)]. One can see in this case that the fitting approach is even less reliable than the FROG-CRAB method. These results again demonstrate the inaccuracy of the SFA model in the low-energy region for the purpose of retrieving the dipole phase or time delay.

VI. DISCUSSION AND SUMMARY

The examples reported in this article illustrate that for low-energy photoelectrons ($E < 30$ eV), due to the inaccuracy of the SFA model, the FROG-CRAB model can only retrieve the photoionization time delay qualitatively. On the other hand, for high-energy photoelectrons such as in the experiment by Schultze *et al.*, where an XUV pulse centered at 106 eV was used, the SFA is quite adequate. In this circumstance, the dipole phase (time delay) retrieved using FROG-CRAB can be treated as the dipole phase (time delay) of the XUV photoionization alone. Ideally the retrieved results should be independent of the IR and the XUV used. However, at high photoelectron energies, the dipole phase is relatively flat with respect to the energy, thus the retrieved dipole phase will be sensitive to any inaccuracy resulting from the FROG retrieval algorithm, especially if the XUV has some degree of chirp. Underlying this difficulty is the fact that the spectrogram is much less sensitive to the dipole phase of the target than to the phase of the XUV pulse. In view of this difficulty, the time delay of 21 as reported by Schultze *et al.* may contain intrinsic errors in the retrieval process. To contradict this speculation, future experiments should use different XUV (with small chirps) and IR pulses to demonstrate the stability of the retrieved dipole phase difference or time delay. Moreover, the FROG-CRAB method imposes a limitation on the XUV bandwidth. For broadband XUV pulses the central momentum approximation used in the FROG-CRAB method would fail. As an alternative we have proposed a procedure based on fitting to retrieve the dipole phase of an unknown target using a well-known reference target, which is applicable for XUV pulses with a broad bandwidth.

In summary, we have examined the controversial time delay issue in recent attosecond XUV photoionization streaking experiments. We have identified the conditions and demonstrated how the FROG-CRAB can be used to retrieve the phase of the transition dipole in such experiment. Due to the insensitivity of the spectrogram to the atomic dipole phase and due to the central momentum approximation, accurate retrieval of the dipole phase is difficult unless the XUV is nearly transform-limited and the spectral bandwidth of the XUV is not too broad. Under the most favorable conditions, FROG-CRAB can give the phase difference between two transition dipoles as a function of the photon energy.

The absolute phase cannot be determined by the FROG-CRAB method, while its first-order energy derivative is defined in terms of a Wigner-like time delay [see Eq. (9)]. This time delay is actually remotely related to the original time delay

defined by Wigner for a stationary system. The transition dipoles, defined in Eqs. (9) and (10), are for photoelectrons emerging in the direction of the polarization axis. The electron wave packet generated by XUV photoionization alone is given by $\chi(t)$ in Eq. (13) or by $\tilde{\chi}(E)$ in Eq. (14), in the time domain and in the energy domain, respectively. Only by analyzing the whole electron wave packet can one draw a conclusion about the time information of the photoelectrons. The Wigner-like time delay defined in Eq. (11), taken at the peak energy of the wave packet, can be understood as the group delay of the electron wave packet only when the XUV pulse is transform-limited. The time delay thus defined does not convey the notion of the delay of a photoelectron reaching the detector directly. While a large Wigner time delay may imply a slowdown of the electron wave packet after it leaves the atom, such a slowdown cannot be measured experimentally, especially on the attosecond time scale with conventional detectors. In fact, a similar "slowdown" occurs when light travels through a dispersive medium. A group velocity (or an index of refraction) can be defined if the dispersion is small. When the medium is highly dispersive, the group velocity alone cannot describe the motion of the wave packet. In this case, a full characterization of the spectral phase is needed. In the same vein, for the streaking experiment, it is the spectral phase of the electron wave packet generated by the XUV pulse that is retrieved. This information will enable the full characterization of the complex electron wave packet including its time dependence in the coordinate space. But using a single time delay to represent the whole electron wave packet is an oversimplification. This oversimplification is one of the main reasons for the existing (unnecessary) debates, especially when the "delay" is of the order of a few tens of attoseconds or less. In this work, we do not address time delays directly extracted from examining the shift of the peak position in the spectrogram. Since the XUV and the IR pulses are not accurately known in any streaking experiments, to extract information about the dynamics of the system would require the simultaneous extraction of these laser parameters.

[1] L. Eisenbud, Ph.D. thesis, Princeton University, 1948.

[2] E. P. Wigner, Phys. Rev. **98**, 145 (1955).

[3] F. T. Smith, Phys. Rev. **118**, 349 (1960).

[4] R. Pazourek, S. Nagele, and J. Burgdörfer, Rev. Mod. Phys. **87**, 765 (2015).

[5] M. Drescher *et al.*, Nature (London) **419**, 803 (2002).

[6] G. Sansone *et al.*, Science **314**, 443 (2006).

[7] A. L. Cavalieri *et al.*, Nature (London) **449**, 1029 (2007).

[8] G. Sansone *et al.*, Nature (London) **465**, 763 (2010).

[9] M. Schultze *et al.*, Science **328**, 1658 (2010).

[10] S. Neppl, R. Ernstorfer, E. M. Bothschafter, A. L. Cavalieri, D. Menzel, J. V. Barth, F. Krausz, R. Kienberger, and P. Feulner, Phys. Rev. Lett. **109**, 087401 (2012).

[11] M. Sabbar, S. Heuser, R. Boge, M. Lucchini, T. Carette, E. Lindroth, L. Gallmann, C. Cirelli, and U. Keller, Phys. Rev. Lett. **115**, 133001 (2015).

[12] A. S. Kheifets and I. A. Ivanov, Phys. Rev. Lett. **105**, 233002 (2010).

[13] L. R. Moore, M. A. Lysaght, J. S. Parker, H. W. van der Hart, and K. T. Taylor, Phys. Rev. A **84**, 061404 (2011).

[14] S. Nagele, R. Pazourek, J. Feist, and J. Burgdörfer, Phys. Rev. A **85**, 033401 (2012).

[15] J. M. Dahlström, T. Carette, and E. Lindroth, Phys. Rev. A **86**, 061402 (2012).

[16] A. S. Kheifets, Phys. Rev. A **87**, 063404 (2013).

[17] J. Feist, O. Zatsarinny, S. Nagele, R. Pazourek, J. Burgdörfer, X. Guan, K. Bartschat, and B. I. Schneider, Phys. Rev. A **89**, 033417 (2014).

[18] J. M. Dahlström, A. L'Huillier, and A. Maquet, J. Phys. B: At. Mol. Opt. Phys. **45**, 183001 (2012).

[19] A. Maquet, J. Caillat, and R. Taïeb, J. Phys. B: At. Mol. Opt. Phys. **47**, 204004 (2014).

[20] Y. Mairesse and F. Quéré, Phys. Rev. A **71**, 011401 (2005).

[21] V. S. Yakovlev, J. Gagnon, N. Karpowicz, and F. Krausz, Phys. Rev. Lett. **105**, 073001 (2010).

[22] M. Kitzler, N. Milosevic, A. Scrinzi, F. Krausz, and T. Brabec, Phys. Rev. Lett. **88**, 173904 (2002).

[23] X. M. Tong and C. D. Lin, J. Phys. B: At. Mol. Opt. Phys. **38**, 2593 (2005).

[24] H. Wei, A. T. Le, T. Morishita, C. Yu, and C. D. Lin, Phys. Rev. A **91**, 023407 (2015).

[25] C. D. Lin, Phys. Rev. A **9**, 171 (1974).

[26] D. Kane, IEEE J. Quantum Electron. **35**, 421 (1999).

[27] J. Gagnon, E. Goulielmakis, and V. S. Yakovlev, Appl. Phys. B **92**, 25 (2008).

[28] R. López-Martens *et al.*, Phys. Rev. Lett. **94**, 033001 (2005).

[29] J. W. Cooper, Phys. Rev. **128**, 681 (1962).

[30] D. L. Carroll, FORTRAN genetic algorithm driver (1999); http://www.cuaerospace.com/Technology/GeneticAlgorithm/GADriverFreeVersion.aspx.

[31] R. H. Garvey, C. H. Jackman, and A. E. S. Green, Phys. Rev. A **12**, 1144 (1975).

[32] Z. Chen, T. Morishita, A. T. Le, M. Wickenhauser, X. M. Tong, and C. D. Lin, Phys. Rev. A **74**, 053405 (2006).

[33] T. Morishita, Z. Chen, S. Watanabe, and C. D. Lin, Phys. Rev. A **75**, 023407 (2007).